



Research paper

Experimental proof-of-concept of HelioSea: A novel marine floating photovoltaic device

Rubén Claus^{a,*}, Fernando Soto^a, Alejandro Cebada^a, Mario López^a, Daniel Clemente^{b,c}, Gianmaria Giannini^{b,c}, Paulo Rosa-Santos^{b,c}

^a DyMAST Research Group and Department of Construction and Manufacturing Engineering, University of Oviedo, Polytechnic School of Mieres, 33600, Mieres, Asturias, Spain

^b Department of Civil Engineering, Faculty of Engineering of the University of Porto (FEUP), rua Dr. Roberto Frias, s/n, 4200-465, Porto, Portugal

^c Interdisciplinary Centre of Marine and Environmental Research of the University of Porto (CIIMAR), Terminal de Cruzeiros de Leixões, Av. General Norton de Matos s/n, 4450-208, Matosinhos, Portugal



ARTICLE INFO

Keywords:

Floating photovoltaic
Tension leg platform
Offshore solar
Response amplitude operators
Marine renewable energy
Physical modelling

ABSTRACT

Floating photovoltaic (FPV) plants have seen rapid growth during the last decade. Currently, the technological challenge lies in developing technology to transition from freshwater to the vast and untapped marine environment. This paper outlines the first experimental proof of concept of HelioSea, an innovative floating photovoltaic system. The device includes a pole-mounted solar platform with a double-axis tracker, supported by a tension-leg platform. A 1:30 scale model was tested at the wave basin of the University of Porto to assess its response to regular and irregular waves. In total, 27 regular wave tests were conducted to establish the Response Amplitude Operators (RAOs) of the structure. The device showed a low amplitude response in all degrees of freedom for $T < 20$ s, featuring surge responses of up to 4 m/m and yaw responses of up to 1 deg/m. The captured surge natural period aligned with initial estimations at $T = 24$ s. Additionally, short- and long-crested irregular wave tests were performed to confirm its response in more realistic scenarios. The resulting irregular motion transfer functions confirmed the stability of the proposed concept. Design considerations for the future developments of HelioSea are provided based on the insights gained from these tests.

1. Introduction

Floating photovoltaic (FPV) plants have been successfully deployed on inland water bodies over the past decade, doubling the installed power each year (Cazzaniga and Rosa-Clot, 2021). This remarkable growth can be explained, in part, by some benefits associated with energy efficiency. The cooling effect of water enhances the efficiency of PV modules (Ueda, 2008). Moreover, water bodies inherently minimize shadows cast on PV modules, and experience higher wind speeds – two aspects that contribute to maximizing electricity generation (Elminshawy et al., 2021; Kazem et al., 2017). The presence of water also facilitates the regular cleaning of PV modules (Mani and Pillai, 2010). Even so, inland water bodies may not suffice to meet the ambitious energy transition goals that are currently set for the upcoming decades (López et al., 2022).

As this renewable energy matures, current research efforts are focused on developing FPV systems for the marine environment

(Oliveira-Pinto and Stokkermans, 2020). The vast and untapped marine space could provide clean energy access to populations with limited available land. However, the harsh marine conditions may compromise the survivability of FPV plants and their electricity generation, potentially leading to more expensive designs. In addition, the marine environment entails other drawbacks such as higher installation costs, more intricate operation and maintenance, navigational hazards, overlap with marine space usage, and unidentified environmental impacts. Conversely, on a positive note, the cooling effect may increase, and the losses due to the casting of shadows vanish, resulting in a higher generation efficiency compared to onshore systems. Moreover, marine FPV plants may synergize with other renewable energies such as offshore wind (López et al., 2020), but also with other marine activities such as oil and gas platforms, aquaculture, desalination, and port activities (Rosa-Santos et al., 2022).

Some marine FPV devices have already been deployed and others are currently being researched. The first offshore solar project was developed by a Dutch consortium under the name Zon op Zee, which

* Corresponding author.

E-mail address: clausruben@uniovi.es (R. Claus).

<https://doi.org/10.1016/j.oceaneng.2024.117184>

Received 14 November 2023; Received in revised form 31 January 2024; Accepted 17 February 2024

Available online 10 March 2024

0029-8018/© 2024 The Authors. Published by Elsevier Ltd. This is an open access article under the CC BY-NC license (<http://creativecommons.org/licenses/by-nc/4.0/>).

List of abbreviations

A –	Added mass matrix	M –	Mass matrix
C –	Normalization constant	n –	Directional spreading
C_H –	Hydrostatic stiffness matrix	PV –	Photovoltaic
CoB –	Centre of buoyancy	RAO –	Response Amplitude Operator
CoG –	Centre of gravity	Re –	Reynolds number
d –	Draft [m]	RMSE –	Root Mean Square Error
D –	Characteristic dimension of a structural element [m]	std –	Standard deviation
DoF –	Degree of freedom	T –	Wave period [s]
E –	Elastic modulus	T₀ –	Initial mooring line tension [N]
E_I –	Incident wave energy [J]	T_p –	Wave peak period [s]
E_R –	Reflected wave energy [J]	t –	Time [s]
f –	Frequency [Hz]	TLP –	Tension Leg Platform
FPV –	Floating Photovoltaic	TRL –	Technology Readiness Level
H –	Wave height [m]	UV –	Ultraviolet
H_s –	Significant wave height [m]	WP1 to WP7 –	Wave probe 1 to wave probe 7
I_{xx} –	Moment of inertia around the x-axis [kg · m ²]	η –	Water surface elevation [m]
I_{yy} –	Moment of inertia around the y-axis [kg · m ²]	γ –	Peak enhancement factor
I_{zz} –	Moment of inertia around the z-axis [kg · m ²]	λ –	Scale factor
K_M –	Stiffness matrix of the mooring system	Γ –	Reflection coefficient
L –	Wavelength [m]	θ –	Wave propagation direction [deg]
L_m –	Mooring line length [m]	θ₀ –	Main wave propagation direction [deg]
		ω_n –	Natural angular frequency vector [rad/s]

launched a rigid FPV platform in the North Sea in 2019 (Oceans of Energy, 2020). OceanSun proposed a flexible design based on a thin membrane that adapts to the oncoming waves, aiming to minimize material usage and the subsequent cost of energy (Ocean Sun, 2017). Alternatively, a semi-rigid modular approach, involving floating arrays of semi-submersible platforms has been proposed by different developers such as Solar Duck (Solar Duck, 2021), CIMC Raffles (Yihe, 2023), or Equinor and Moss Maritime (Garanovic, 2021). Recently, a Belgian partnership tested SeaVolt, an offshore rigid semi-submersible solar platform (DEME et al., 2023). Despite the increasing number of marine FPV developers, there is still a lack of consensus on a standardized technology.

On these grounds, there is a need for research and development efforts to design cost-effective structures capable of withstanding extreme environment loads while providing a stable platform for supporting PV panels (Claus and López, 2022). The importance of stability requirement cannot be overstated, as the rotational motions of the FPV system result in the misalignment of the solar panels, causing a subsequent reduction in the plane of the array irradiance (Bugeja et al., 2021). These misalignments are noticeable in the most common pontoon-type FPV technologies. An experimental study recorded pitch amplitudes of up to 15 deg in a multibody FPV system under wave heights below 1 m (Delacroix et al., 2023). The same maximum pitch motions were numerically estimated in a similar FPV design (Ikhennicheu et al., 2022).

A comprehensive assessment of the wave-induced motions is crucial during the development of an FPV system (Claus and López, 2023). While numerical and physical models can serve this purpose, the latter are indispensable to reliably ascertain the system's response to wave conditions. For example, a 1:60 scaled model of a soft-connected multibody array designed specifically for offshore conditions was analysed in a testing channel, with wave heights of up to 10 m in model scale (Jiang et al., 2023). A prototype scale multibody articulated FPV system was tested in a wave tank, for waves of up to 0.5 m (Delacroix et al., 2023). A 1:4.5 scale Gable Slender FPV was investigated experimentally in a wave flume for waves of up to 1 m in model scale (Friel et al., 2023). A rigid FPV platform was tested through a 1:4 scaled model under waves of up to 0.75 m and winds of up to 25 m/s in model scale at a wave-wind basin (Yang and Yu, 2021).

This work presents, for the first time, the experimental testing of HelioSea, an innovative offshore FPV design that is being developed by researchers of the University of Oviedo (Spain). The concept aims to maximize the overall electricity generation and provide a resistant platform to hold the PV panels. This double objective is reached by combining two key elements: a double-axis solar tracking system, and a Tension-Leg Platform (TLP) (Fig. 1). The latter is designed to ensure the structure's stability, which is of utmost importance, as it serves to both minimize losses arising from panel misalignment and enable the functionality of the tracking systems. To demonstrate the concept and push the TRL upward (from TRL 1 to TRL3), a 1:30 scale model was tested at the wave basin of the University of Porto (Portugal).

The remainder of this paper is structured as follows. Section 2 discloses the conceptual design, describes the physical model as well as the testing facilities, explains the experimental layout and measuring devices, and presents the testing programme and conditions. Section 3 presents and discusses the results gathered from the regular and irregular wave tests, along with an examination of the influence of various factors on these results. Finally, in Section 4, conclusions are drawn, summarized, and presented.

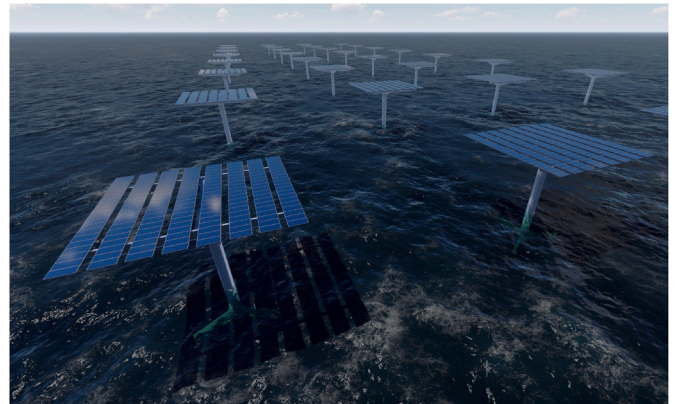


Fig. 1. Computer-generated imagery of HelioSea.

2. Materials and methods

2.1. Conceptual design

The tested marine FPV concept, HelioSea, consists of two elements (Fig. 2):

- a superstructure, composed of a pole-mounted solar platform, with a double-axis tracker to maximize productivity through panel alignment with solar irradiance; and
- a substructure, which consists of a cylindrical float, that provides the required buoyancy, and a tension-leg platform (TLP) that ensures the anchoring, survivability, and stability of the structure.

The superstructure is based on the top-of-pole solar panel designs used in well-developed terrestrial photovoltaic plants. A post, roughly 10 m tall, rises from the floating cylinder and is bifurcated at the top to form a Y-shaped structure that supports two horizontal beams. These beams support the 6 rows of PV modules, which are held in place by pairs of rails. This device can hold 6 rows of 23 PV modules (138 in total), resulting in a $12 \times 24 \text{ m}^2$ platform with a 75-kW rated power. A vertical tracking system to significantly increment energy production can be accommodated at the highest point of the post, while a horizontal tracker, consisting of a piston-activated cylinder, can be installed between the post and the furthest row of PV modules. Secondary appliances, such as signal processing units, sensors, motion control modules, or power supply systems may be accommodated in the superstructure.

The substructure is a TLP, which is a system that was developed for offshore floating platforms used for oil and gas extraction. TLPs have also been used in more recent offshore wind turbines (Oguz et al., 2018). The studied TLP consists of 4 pontoons forming a cross layout and a

cylindrical float that rises from the centre of the cross. The system's buoyancy is driven by the cylindrical float, and should greatly exceed the total weight of the device. The device is partially submerged by the mooring system, which consists of 4 vertical cables in permanent tension, connected to each pontoon endpoint. This configuration partially allows surge, sway, and yaw motions, but heavily restricts pitch, heave, and roll motions. The structural elements of the device are meant to be made of steel but other materials, such as fibre-reinforced plastics, could be explored in the future.

HelioSea, which was designed for the marine environment, presents several unique advantages when compared to other FPV designs:

- The dual-axis tracking system maximizes the amount of direct normal irradiance striking the PV modules, resulting in superior production. The energy return of single-axis and double-axis trackers may be 25% and 40% more, respectively, when compared to the fixed PV systems (Nsengiyumva et al., 2018).
- The slender approach results in small wave forces, allowing the structure to endure harsh wave conditions. The mooring lines of the TLP will restrict pitch and roll motions, thus minimizing panel misalignment losses. Heave motions are also minimal, which could prove valuable for easier maintenance.
- The top-of-pole design keeps the PV modules at an emerged height of, at least, 5 m. This is a distinguishing feature of HelioSea that keeps the PV modules safe from potential wave slamming, overtopping, and splashing.
- This design synergizes with the use of bifacial panels, given the height at which they are installed (Sun et al., 2018). Tina et al. (2021) reported bifacial gains of up to 13.5% for an FPV design without a tracking system.

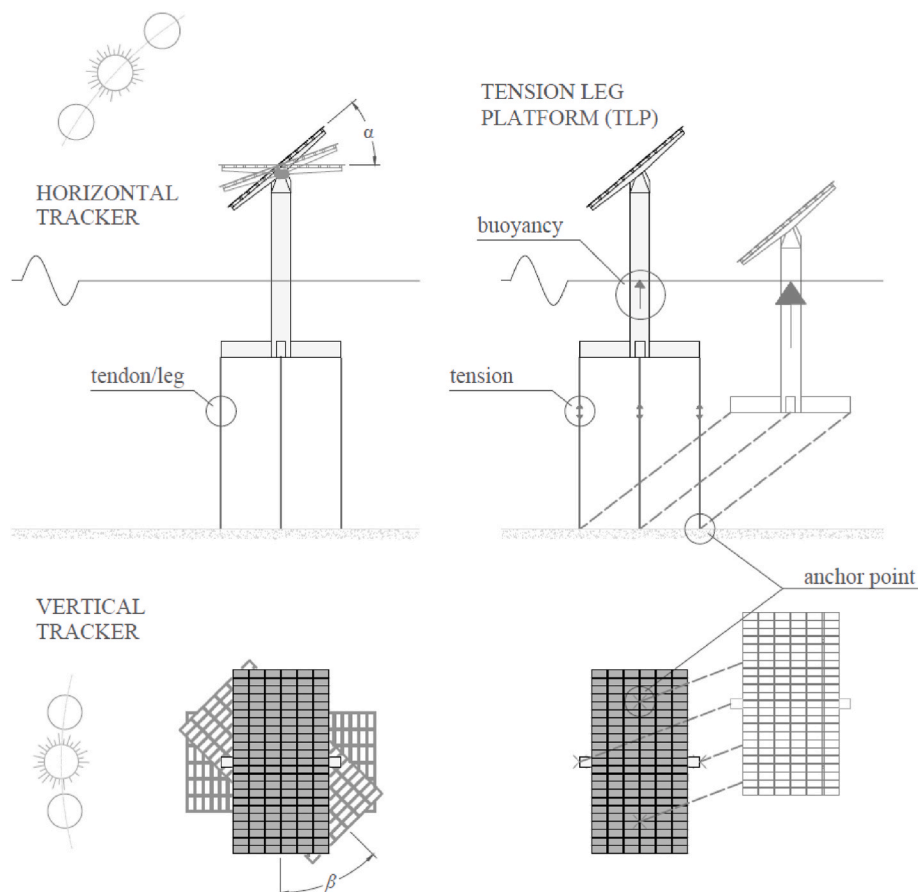


Fig. 2. Schematics of the conceptual design, with details of the dual-axis tracking system and the TLP.

- The height at which the PV modules are installed should increase wind exposure, which will also increase the cooling effect, positively impacting both the efficiency and the durability of the PV modules (Sun et al., 2017).

This technology does, however, have some technical challenges:

- The installation of HelioSea’s mini TLP may pose complications. To streamline this process, a ballast barge can be employed to mitigate excess buoyancy, facilitating an easier towing operation. Hook-up can be performed on land to a pre-sunk monolithic foundation platform, with the final step involving the removal of ballast to tighten mooring lines.
- Maintenance operations, especially cleaning of the PV modules, will be more difficult due to the height. This may be avoided if automated cleaning and cooling methods, such as water veil cooling (Cazzaniga et al., 2018), were to be deployed.
- The increased wind exposure will result in additional loading. However, the tracking system doubles as a defence mechanism, and can adopt a survival configuration to minimize exposure during extreme wind loads.
- HelioSea should be designed to withstand diverse degradation mechanisms such as erosion, abrasion, UV-induced deterioration, extreme temperature fluctuations, elevated humidity, and, crucially, saltwater corrosion. Fabrication requires rigorous surface preparation, followed by a dual-layer protective system involving hot-dip galvanization and a suitable coating applied to each steel member. Future development may consider alternative materials like fibre-reinforced polymers.
- The mooring lines are vulnerable to fatigue damage over their design life period due to the dynamic excitations caused by the oscillating waves and wind (Siddiqui and Ahmad, 2001). This aspect must be addressed in future developments of HelioSea.

2.2. Scale of the physical model

The proposed concept allows multiple configurations and, therefore, a simplified initial reference design was defined for testing. To properly model the device, the scale reduction must satisfy kinematic and dynamic similarity to a reasonable degree (Hughes, 1993). There are two approaches to fulfilling the similarity criteria, which are based on conserving the Reynolds number or the Froude number. Ideally, the prototype and scaled designs should conserve both factors. However, conforming to one dimensionless factor usually results in neglecting the other. Nonetheless, if the Reynolds number is kept sufficiently large ($Re > 10^5$), the flow could be considered turbulent, and some non-linear effects could be neglected (Sheng, 2019). For these tests, the Froude approach was selected, using a scale of $\lambda = 1:30$, which was the maximum scale that the facility permitted, to minimize scale and model effects. The Reynolds number was verified to be $Re > 10^5$ for every test

Table 1
Scale factors for the different magnitudes according to Froude similarity criteria.

Magnitude	Units	Scale factor
Length	m	λ
Area	m ²	λ^2
Volume	m ³	λ^3
Moment of inertia	m ⁴	λ^4
Mass	kg	λ^3
Time	s	$\lambda^{1/2}$
Frequency	s ⁻¹	$\lambda^{-1/2}$
Displacement	m	λ
Velocity	m/s	$\lambda^{1/2}$
Acceleration	m/s ²	1
Rotation	deg	1
Angular velocity	deg/s	$\lambda^{-1/2}$
Angular acceleration	deg/s ²	λ^{-1}

case. The scale factors for the most relevant magnitudes are depicted in Table 1.

2.3. Description of the physical model

The model device consists of the following parts (Fig. 3):

- A welded steel frame that replicates the post, as well as the 4 pontoons that make up the cross component of the device.
- A cylinder of extruded polystyrene that provides buoyancy to the model and replicates the cylindrical float.
- A wooden board that replicates the platform where the PV modules of the device are installed. This board was also used to accommodate the markers required for the motion-capturing system, which is described in Section 2.5.
- 4 steel wires, which replicate the mooring system of the device.
- A steel base, with preinstalled connection points, that replicate the seabed and the anchoring points.

The main dimensions and masses of the components of the model are summarized in Fig. 4 and Table 2. The elastic modulus of steel was assumed to be $E = 210$ GPa. Note that a rod was later allocated on top of the device to accommodate a marker for the motion capture system.

The inertia, mass, and buoyancy properties of the model are summarized in Table 3. For the inertia, note that x corresponds to the direction of the waves and z corresponds to the direction of gravity. The centre of gravity (CoG) and the centre of buoyancy (CoB) are in the axis of the post of the model and lie at the indicated height from the base. The pretension of each mooring line was 6.4 N.

The avoidance of resonance is of paramount importance in the design of TLPs. The dynamics of HelioSea can be investigated by examining the subsequent equation, which describes the natural frequencies of an undamped single degree of freedom (DoF) system:

$$\omega_n = \sqrt{\frac{C_H + K_M}{M + A}}, \tag{1}$$

Where C_H is the hydrostatic stiffness matrix, K_M is the stiffness matrix of the mooring system, M is the mass matrix and A is the added mass matrix. The primary contributor to stiffness is the mooring lines. The mooring stiffness matrix for each tendon can be estimated in the following form:

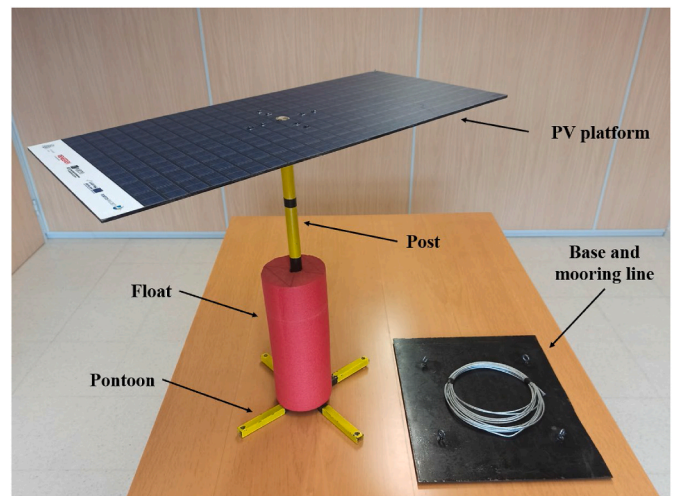


Fig. 3. Parts of the experimental model.

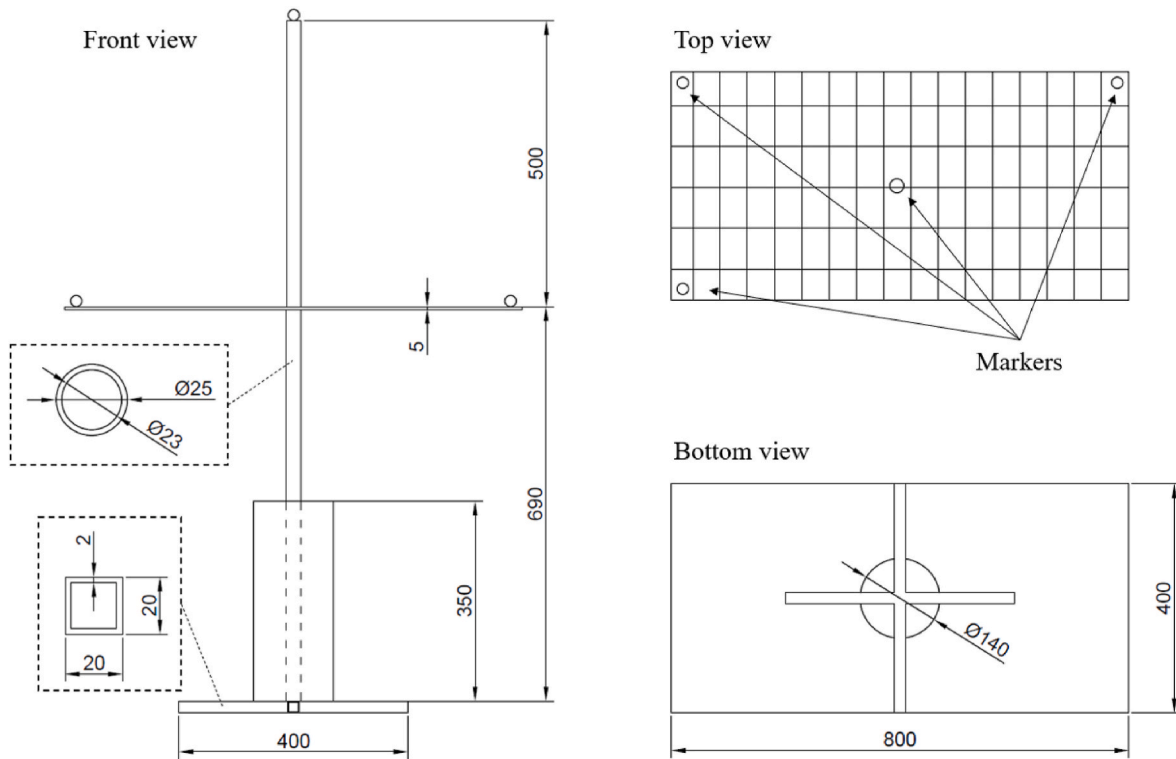


Fig. 4. Dimensions of the physical model (units in mm).

Table 2
Mass and dimensions of the components of the physical model.

Component	Mass (g)	Dimensions	
Post	780	Length (mm)	690
		Diameter (mm)	25
		Thickness (mm)	2
Float	250	Length (mm)	350
		Diameter (mm)	140
Pontoons	500	Length (mm)	200
		Section (mm ²)	20 × 20
		Thickness (mm)	2
Cable	75	Length (mm)	1500
		Diameter (mm)	3
Board	845	Section (mm ²)	400 × 800
		Thickness (mm)	5

Table 3
Inertia, mass, and buoyancy properties of the model.

Property	Unit	Value
I_{xx}	g·m ²	240
I_{yy}	g·m ²	240
I_{zz}	g·m ²	70
Mass	g	2675
CoG height	m	0.38
Displacement	dm ³	5.4
CoB height	m	0.18
Draft (d)	m	0.53
Excess buoyancy	dm ³	2.73

$$\mathbf{K}_M = \begin{bmatrix} \frac{T_0}{L_m} & 0 & 0 & 0 & -d \frac{T_0}{L_m} & 0 \\ 0 & \frac{T_0}{L_m} & 0 & d \frac{T_0}{L_m} & 0 & 0 \\ 0 & 0 & \frac{EA_m}{L_m} & 0 & 0 & 0 \\ 0 & d \frac{T_0}{L_m} & 0 & y_m^2 \frac{EA_m}{L_m} & 0 & 0 \\ -d \frac{T_0}{L_m} & 0 & 0 & 0 & x_m^2 \frac{EA_m}{L_m} & 0 \\ 0 & 0 & 0 & 0 & 0 & (x_m^2 + y_m^2) \frac{T_0}{L_m} \end{bmatrix}, \quad (2)$$

where T_0 is the pretension of the mooring lines, E is the elastic modulus, A_m is the cross-section, x_m and y_m are the coordinates of the fairlead in a Cartesian system centred in the axis of the structure and L_m is the length of the mooring line. The mooring stiffness matrix reveals that this structure is a soft spring in surge, sway and yaw motions, but stiff in heave, roll and pitch motions. The soft natural frequencies can be tuned by modifying mooring line length, fairlead position, buoyancy excess, mass, inertia and added mass. The natural frequencies were estimated for the structure and can be seen in Table 4. These were computed through the linear approximations proposed by Bachynski and Moan (2012), using the parameters presented in in Tables 2 and 3. It is

Table 4
Estimated natural frequencies of HelioSea.

Motion	Natural frequency (prototype scale)
Surge	0.04 Hz
Sway	0.04 Hz
Heave	5.42 Hz
Roll	2.20 Hz
Pitch	2.20 Hz
Yaw	0.06 Hz

particularly important to keep sway and surge natural frequencies beyond the first-degree wave excitation regime since TLP designs require restricting translational excursions to ensure that mooring line angles remain below 10 deg (Chakrabarti, 2005).

2.4. Testing facilities

The model was tested at the wave basin of the Hydraulics, Water Resources and Environment Division of the Faculty of Engineering of the University of Porto. It features a $12 \times 28 \times 1.2 \text{ m}^3$ wave basin equipped with a wavemaker system (HR Wallingford), composed of 16 piston-type wave paddles (Fig. 5). These can be activated by its control unit to reproduce regular, irregular long-crested or irregular short-crested waves, including sea-states based on the JONSWAP spectrum. A central pit enables an additional 1.4 m of depth, which is of particular interest for floating moored bodies such as HelioSea. Due to the scale of the model and the limitations of the facilities, the pit of the basin was required to extend the mooring lines of the device. This approach has already been successfully implemented to test floating devices with similar scale and wave conditions (Fernandez et al., 2012; Kurniawan et al., 2019; Lavelle and Kofoed, 2011). The model was allocated in the centre of the pit, with its pontoons forming a 45 deg angle with the incoming wave direction. A dissipating beach, opposite to the wavemaker, promotes parasitic wave dissipation and wall reflection mitigation.

2.5. Experimental setup

The free surface elevation of the water was registered through 7 strategically located resistive-type wave probes (see Figs. 6 and 7). The first three wave probes (WP1, WP2, and WP3) were deployed to perform a reflection analysis. WP4 was allocated between the pit and the dissipating beach, to measure the wave profile after its passage through the device. WP5 and WP6 were allocated at each side of the device, to interpolate the wave height at the location of the device. Finally, WP7 was installed in line with the aforementioned couple, but outside of the pit, to evaluate the influence of the pit in the wave profile. The accuracy of the wave probes was $\pm 0.15 \text{ mm}$.

The motions of the physical model were tracked through the Qualisys motion capture system, employing a three-camera setup at an elevated position (Fig. 8). The overlap between the cameras allowed the system to capture the 6 DoFs motions of the device throughout all tests, without missing information (Fig. 9). Four infra-red markers were attached to the device in two separate horizontal planes, in a non-symmetric, non-overlapping layout. The system was calibrated daily to ensure that the average residuals were below 0.5 mm at all times. The recommendations

of the Qualisys Manual (Qualisys, 2017) were followed to ensure accuracy. The third camera and fourth marker promoted system redundancy and greater result quality.

2.6. Testing programme

2.6.1. Regular waves

Regular wave tests were performed to characterize the hydrodynamic response and determine the Response Amplitude Operators (RAOs) of the device, as well as to evaluate response linearity with varying wave height. A total of 27 test cases resulted from the combination of 9 wave periods (T) and 3 target wave heights (H). The test conditions can be seen in Table 5. The test cases marked with * were repeated for redundancy. The same test cases were repeated in the absence of the analysed device to assess its influence on the registered wave profiles.

The water depth was 60 cm outside of the pit and 200 cm inside the pit. While the wavemaker could easily provide the requested T , a gain factor was required to obtain the desired H . The number of regular waves generated on each test was 150.

Assuming a characteristic dimension of $D = 4.2 \text{ m}$ in prototype scale and the defined test conditions, the prevailing wave forces were expected to be inertial and drag forces (Fig. 10).

The layout of the installed wave probes within the wave tank allowed for a wave reflection analysis. Even with the presence of the dissipating beach, wave reflection was expected to be relevant in the test cases with the highest wave periods. The reflection coefficient (Γ) is a parameter that describes how much of the wave is reflected at the end of the basin. It was computed through the methodology proposed by Baquerizo (1995) and Mansard and Funke (1980), which separates the incident and reflected wave components through a least-squares approach. To do so, three aligned sensors are required (WP1, WP2, and WP3). Once the incident component has been separated from the reflected component, the reflection coefficient Γ can be computed as the root of the ratio between the reflected wave energy (E_R) and the incident wave energy (E_I):

$$\Gamma = \sqrt{\frac{E_R}{E_I}} \quad (3)$$

In order to reduce disruptions caused by wave reflection, the RAOs were calculated using data captured at the initial stages of the tests. This involved analysing harmonic stable waves and their corresponding motion responses following the ramping process, but prior to the identification of disturbances. The remaining motions were discarded to minimize disturbances specific to the testing facilities.

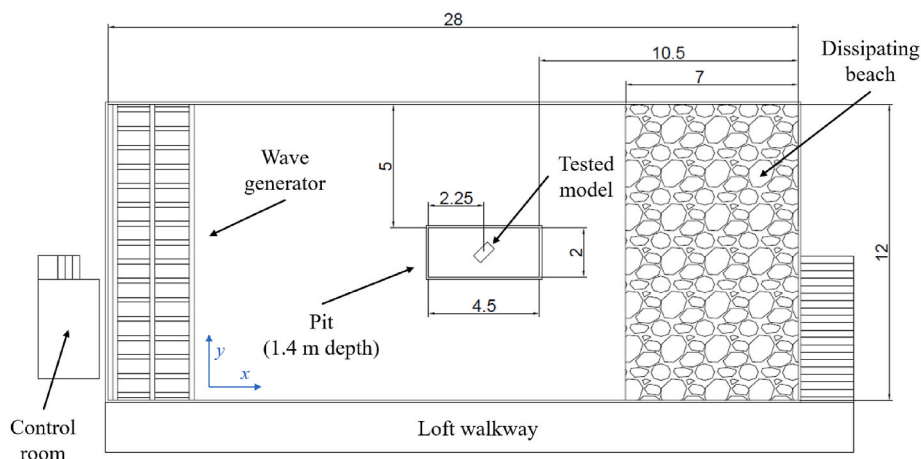


Fig. 5. Schematics of the wave basin (units in m).



Fig. 6. Wave probes and device in the wave basin.

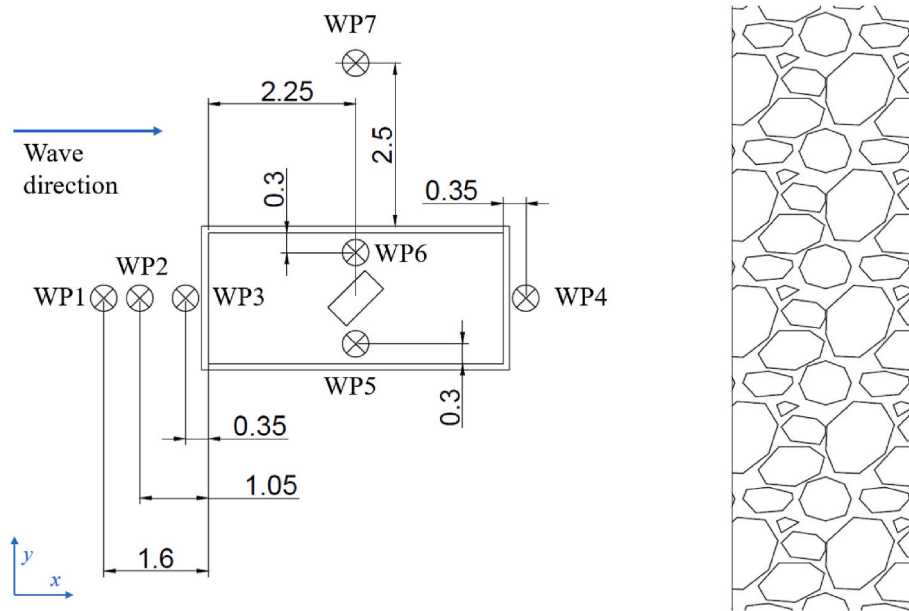


Fig. 7. Layout and naming of the resistive wave probes (units in m).

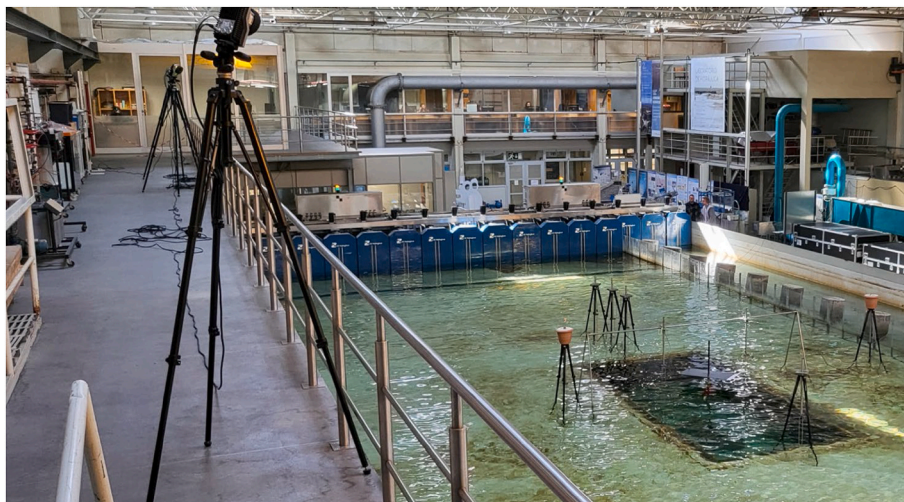


Fig. 8. Installed motion capture cameras pointing at the device.

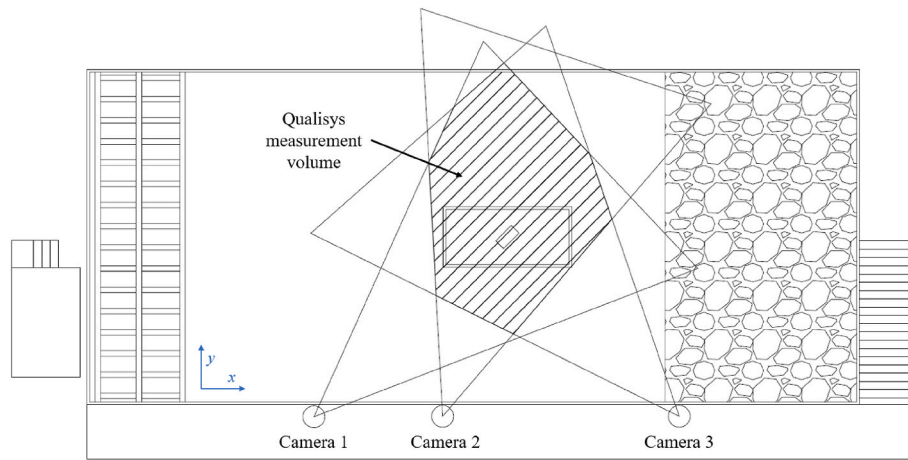


Fig. 9. Layout and measurement volume of the motion capture system.

Table 5
Regular wave test conditions (model scale).

Test case	T (s)	Target H at WP5 (cm)	Registered H at WP5 (cm)	Difference (%)	H at WP1 (cm)	H_I at WP1 (cm)	H_R at WP1 (cm)
R01	0.73	4	3.8	5.0	4.2	4.2	0.2
R02*	1.46	4	4	0.0	4.0	4.0	0.5
R03	2.19	4	3.5	12.5	4.7	4.6	0.5
R04	2.92	4	4.1	2.5	5.9	5.8	0.9
R05*	3.65	4	3.9	2.5	4.8	4.5	0.6
R06	4.02	4	3.8	5.0	5.0	5.0	0.8
R07	4.38	4	3.7	7.5	5.6	4.4	1.2
R08	4.75	4	3.6	10.0	4.4	3.5	1.2
R09	5.11	4	3.8	5.0	5.0	3.7	2.0
R10	0.73	6	5.2	13.3	5.6	5.5	0.4
R11	1.46	6	6.2	3.3	6.2	6.0	1.0
R12*	2.19	6	5.7	5.0	7.8	7.2	1.2
R13	2.92	6	6.2	3.3	8.6	7.9	1.4
R14	3.65	6	6.0	0.0	6.6	6.2	1.3
R15	4.02	6	5.8	3.3	7.8	7.9	1.2
R16*	4.38	6	5.9	1.7	7.4	6.3	1.3
R17	4.75	6	5.7	5.0	6.7	5.3	1.8
R18	5.11	6	5.2	13.3	7.1	5.5	2.0
R19	0.73	8	7.7	3.7	8.2	8.2	0.5
R20	1.46	8	8.2	2.5	8.2	8.0	1.0
R21	2.19	8	7.4	7.5	9.5	9.0	1.2
R22*	2.92	8	8	0.0	9.9	9.8	1.9
R23	3.65	8	8	0.0	8.2	8.0	1.5
R24	4.02	8	7.8	2.5	8.8	8.9	1.4
R25	4.38	8	7.4	7.5	9.5	8.2	1.7
R26	4.75	8	8.2	2.5	7.0	5.5	1.8
R27*	5.11	8	6.8	15.0	8.6	7.2	3.5

The symbol “*” indicates the test cases repeated for redundancy and without the model.

2.6.2. Irregular wave tests

Irregular tests were also carried out to evaluate the device in more realistic environmental conditions and obtain the motion response spectra of the device. The estimation of the motion spectra was performed using the Welch method with 3000 Hamming windows and a 50% overlap. This also allowed the computation of the irregular response transfer functions, which should be similar to the RAOs obtained through the regular wave tests. These transfer functions are the result of the square root of the division of each motion response spectra by their corresponding wave spectra.

Two long-crested wave tests were performed (L01 and L02). These test cases were defined through the governing parameters of the JONSWAP spectrum, namely the significant wave height (H_s), the peak period (T_p), and the peak enhancement factor (γ). This spectrum has already been used in the experimental analysis of other FPV technologies (Delacroix et al., 2023; Friel et al., 2023). The test conditions for the long-crested tests can be seen in Table 6. The remaining test conditions

were kept the same as in the regular wave tests. Wave reflection was assessed with the same approach applied to the regular wave test cases.

Additionally, two short-crested tests (S01 and S02) were performed using adding a direction spreading function to the same test conditions used in the long-crested tests. This function is defined as:

$$D(\theta, f) = C \cos^n\left(\frac{\theta - \theta_0}{2}\right), \tag{4}$$

where C is a normalization constant that ensures the integral of the function over all directions equals one (representing the total wave energy), n is the factor that determines the shape of the spreading function and θ_0 is the mean wave direction. The test conditions for the short-crested tests can also be seen in Table 6. The duration of each irregular test was sufficient to generate at least 500 waves.

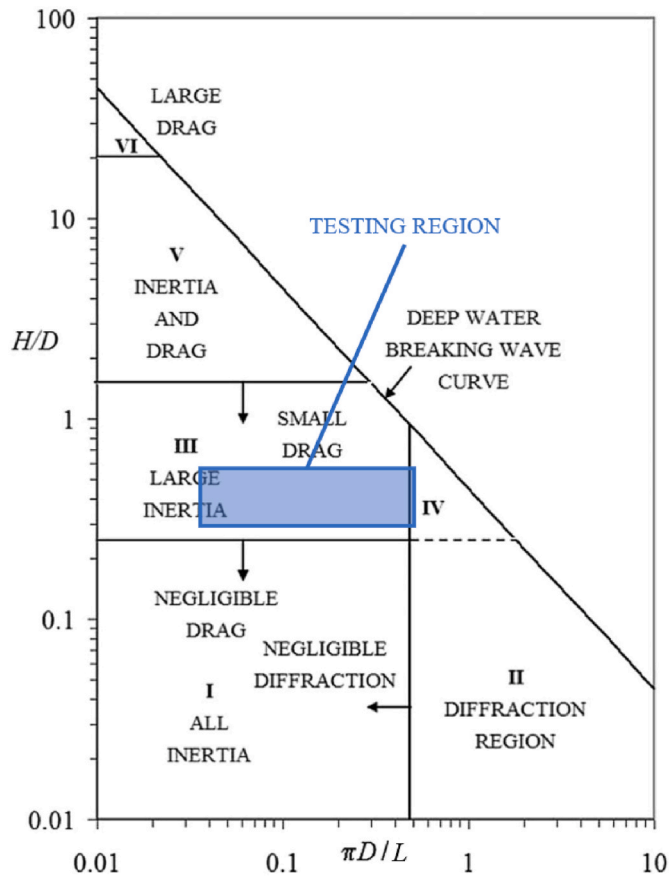


Fig. 10. Wave force regime for the performed regular tests. Adapted from Chakrabarti (1987).

Table 6
Irregular wave test conditions in model values.

Irregular test case	T_p [s]	H_s [cm]	γ	n
L01	2.19	4	3.3	–
L02	3.65	4	3.3	–
S01	2.19	4	3.3	20
S02	3.65	4	3.3	20

3. Results and discussion

3.1. Preliminary analysis

3.1.1. Reflection analysis

A reflection analysis was carried out to prove the effectiveness of the dissipating beach at the end of the basin (Fig. 5) throughout all the performed tests. As a quality measurement, the separated reflected and incident waves were reassembled and compared to the measured wave readings, resulting in an average root-mean-square error (RMSE) < 0.005. The total, incident, and reflected wave heights for regular wave conditions, as measured by WP1, are included in Table 5. The corresponding reflection coefficients case are plotted in Fig. 11.

All the test cases with $T < 24$ s had a $\Gamma < 0.2$, meaning that only a small fraction of the incoming wave was reflected. These coefficients abruptly increase for higher values of T up to a maximum of $\Gamma = 0.56$. This implies that a higher fraction of the long-period waves was reflected instead of dissipated at the beach, and the motions of the device for these test cases will be affected by reflection.

This analysis was also carried out for the irregular long-crested wave tests. For test case L01, the reflection coefficient was $\Gamma = 0.14$, consistent with the values obtained for the regular test cases with similar periods. For test case L02, the reflection coefficient was $\Gamma = 0.29$. This coefficient is higher since the generated wave spectrum contained waves with high values of T .

3.1.2. Influence of the pit

An analysis of the effect of the presence of the pit on the waves is presented in this section. Fig. 12 compares the water surface elevation before the pit, at the pit, and outside the pit for 3 different test cases. These readings correspond to wave probes WP1, WP5 and WP7, respectively, according to Fig. 7. The wave profile seems to be very similar for readings in WP1 and WP7 since they are both outside the pit. In comparison, the readings inside the pit conserve the value of T , but registered a slightly smaller value of H . This subtle distinction emphasizes the necessity of considering the wave height at the device's location (i.e. at WP5 and WP6) for the subsequent computation of the RAOs. Given that these responses are normalized by wave height, this is deemed a minor concern arising from a compromise driven by facility restrictions, in the pursuit of achieving an appropriate scale.

3.1.3. Influence of the presence of the device

The influence of the device on the incoming waves was assessed through additional tests with no device installed (Table 5). The RMSE between the measurements taken by WP4 with the device in place and without it can be seen in Table 7. This value was below 5 % for every test, meaning that the registered waves were very similar regardless of

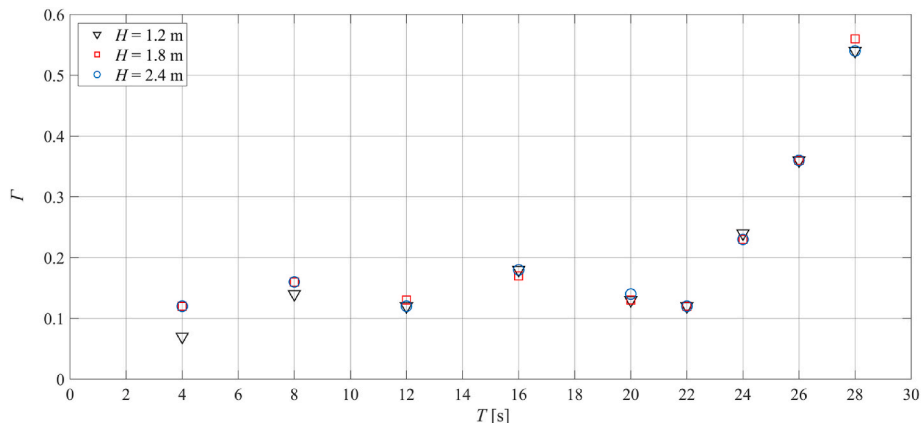


Fig. 11. Reflection coefficients for the analysed test cases.

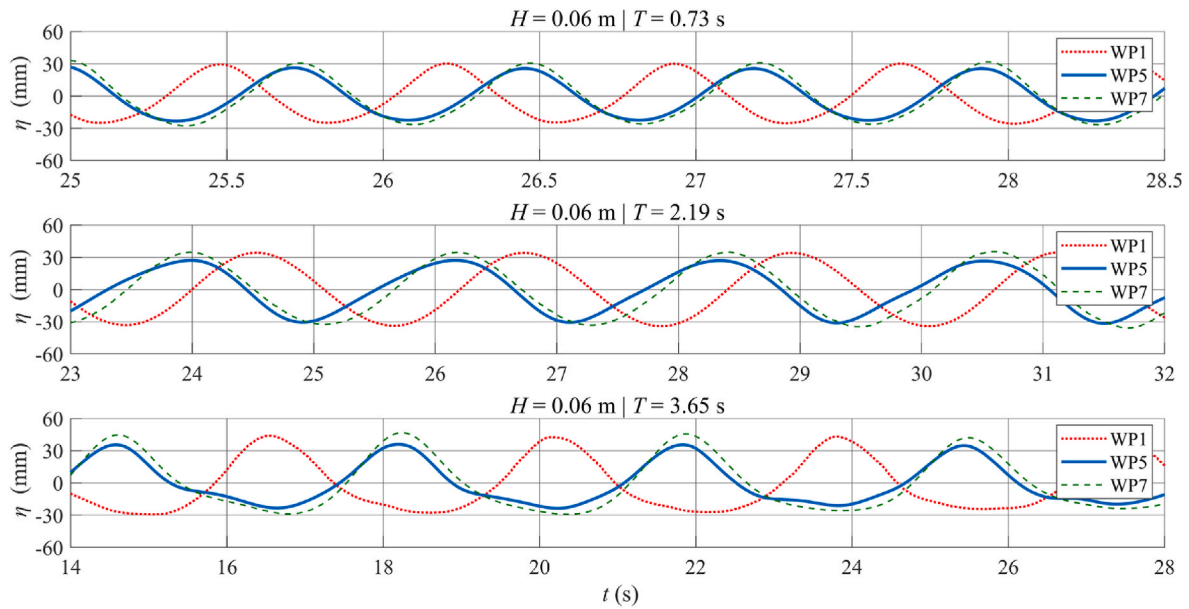


Fig. 12. Water surface elevation before the pit (WP1), inside the pit (WP5), and outside the pit (WP7). All values are on model scale.

Table 7

Influence of the device on the measured H (values in model scale). Relative η RMSE (%) with respect to the measurements in WP4, with the device in place.

Test case	η RMSE (m)	Relative η RMSE (%)
R02	0.06	5.0
R05	0.06	5.0
R12	0.09	5.0
R16	0.08	4.4
R22	0.09	3.8
R27	0.09	3.8

the presence of the device.

3.1.4. Redundancy tests

Redundancy tests were made to assess the reliability of the measurements. The differences measured by WP5 and the surge component of the motions captured by the Qualisys cameras are presented in Table 8. All compared test cases showed a relative RMSE <5%, which confirms the reliability of the experiments.

3.2. Motion response analysis in regular wave tests

A total of 27 test cases were performed to obtain the RAOs of the structure. A summary of the registered average H is shown in Table 5 for every test case. An example of a time series for the water surface elevation (η) as well as the captured motions of the device can be seen in Fig. 13. The wave ramp is discernible, followed by a harmonic variation of the water surface elevation due to the generated regular waves. The

Table 8

Redundancy verification (values in model scale). Relative RMSEs (%) with respect to the original measurements in WP5 and the surge component, respectively.

Test case	Surge RMSE (m)	Relative surge RMSE (%)	η RMSE	Relative η RMSE (%)
R02	0.03	4.6	0.04	3.3
R05	0.11	2.9	0.03	2.5
R12	0.07	2.8	0.01	0.5
R16	0.09	0.9	0.05	2.8
R22	0.22	3.2	0.04	1.8
R27	0.16	1.9	0.04	1.8

translational response of the device shows a dominance of surge motions (x direction, according to Fig. 5), which harmonically oscillate with the frequency of the oncoming waves. The sway motions (y direction, according to Fig. 5) are much smaller while the heave motions are minimal. As for the rotational motions, roll and pitch motions are constrained by the mooring lines, while yaw motions exhibit a minimal amplitude.

The horizontal trajectories of the device for different values of T and $H = 1.2$ m (prototype scale) can be seen in Fig. 14. Similar patterns were found for the different values of H that were tested, hinting a mostly linear behaviour. As observed, the trajectory of the device is very dependent on T . The maximum surge response was measured for $T = 24$ s, as expected, considering the estimated natural surge frequency of the device (0.04 Hz, as depicted in Table 4).

Sway motions were anticipated to be minimal, due to the alignment of the device. However, a deviation from the expected response was measured for $T = 20$ s. In these test cases, the device is demonstrating a pure surge motion, which is later diverted to follow an elliptical trajectory. These deviations may be the consequence of wave reflections against the basin and/or pit contours and therefore were discarded from the analysis, as can be seen in Fig. 14. This phenomenon is barely discernible for test cases different than $T = 20$ s since the device consistently maintained the expected motions.

The RAOs for every regular test case and degree of freedom of the device are shown in Fig. 15. As expected, the surge motion is the most prominent, with values between 0.5 and 7 m/m on prototype scale. The corresponding RAO peaks around $T = 24$ s, which is coherent with the estimated natural frequency (Table 4). The curve does not exhibit a marked peak, i.e. resonance seems to be very limited, probably due to a high damping ratio. The response in this DoF shows consistency across varying wave heights, indicative of linearity. This behaviour is partially lost in the surroundings of the natural frequency, for which the test cases with the lowest value of H present higher RAOs. This trend may be advantageous, since it would entail a reduced response for higher wave heights. The response for common wave conditions ($T < 20$ s) is consistently below 4 m/m. Note that restricting surge motions is essential for ensuring that the mooring line angles remain low and limiting the mooring radius of the device.

The surge natural frequency falls outside of the common frequency range of ocean waves. However, its value is dependent on water depth. In deeper waters, the longer mooring lines will shift the natural

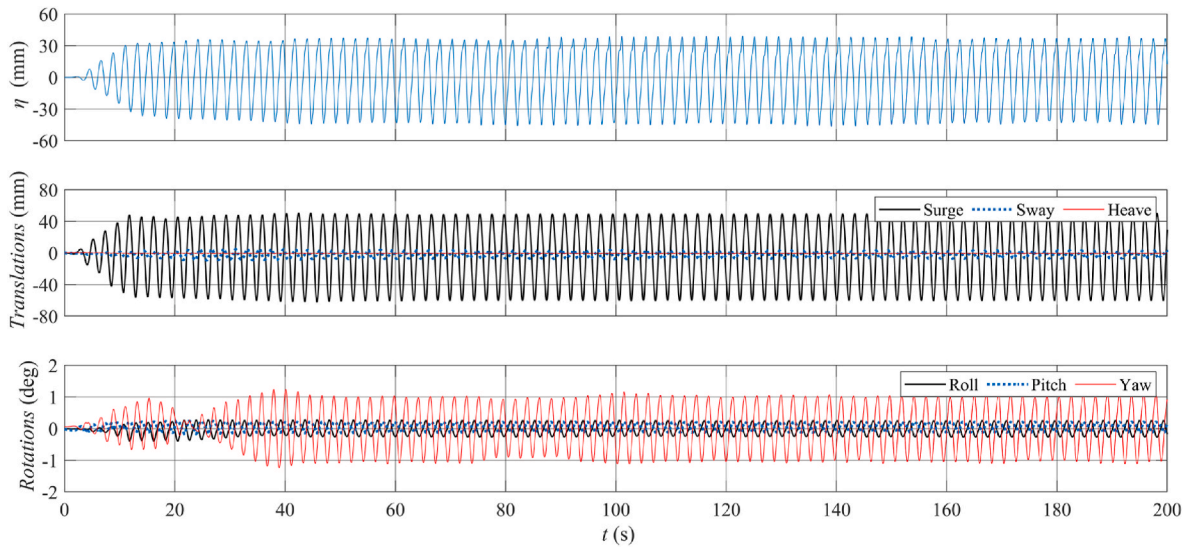


Fig. 13. Water surface elevation (η) and motions of the device for test case R21 (model scale).

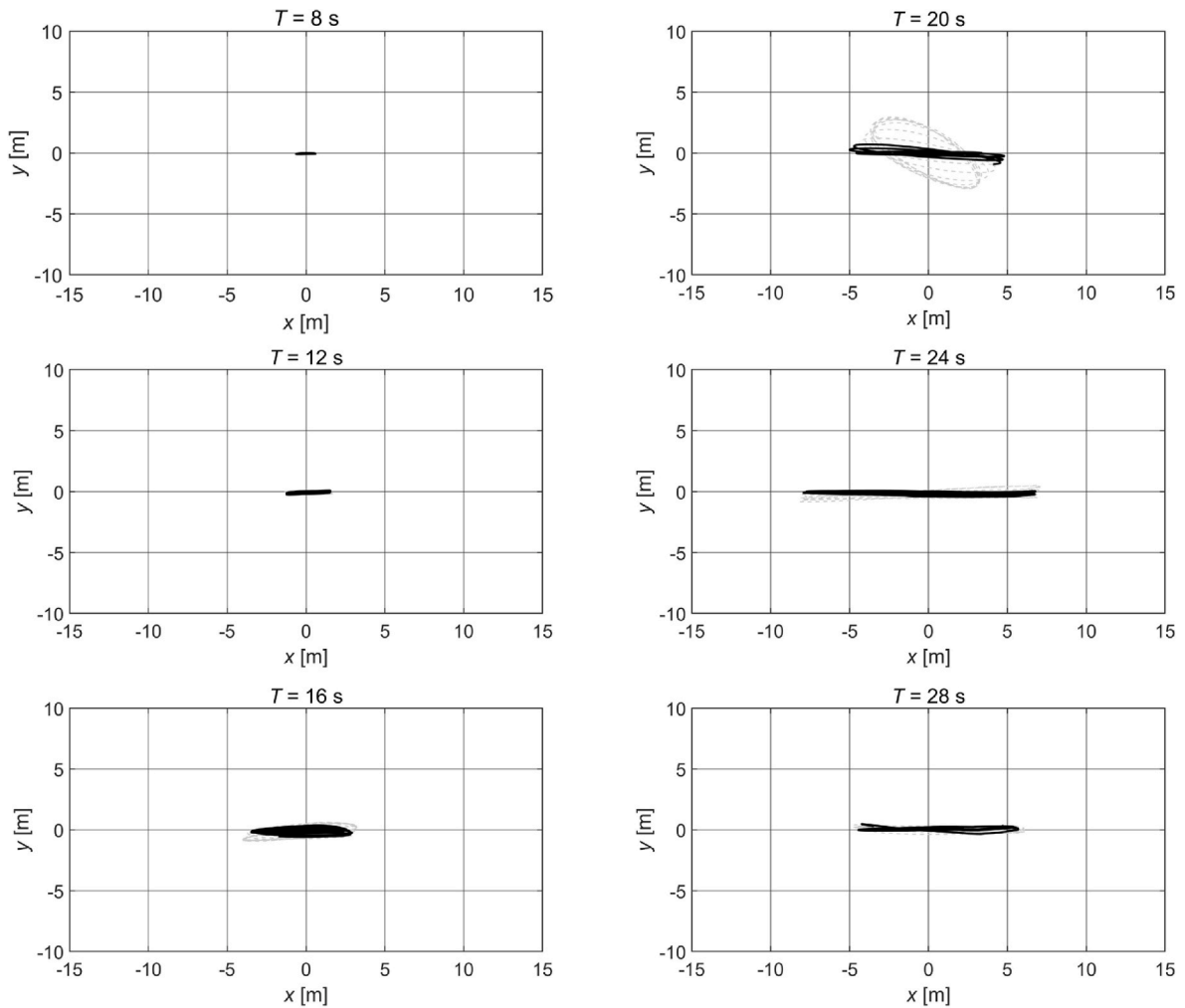


Fig. 14. Trajectories of the device for the regular wave tests for $H = 1.2$ m (prototype scale). The dotted lines represent motions excluded from the analysis.

frequency further away from this range. However, shallower waters will imply shorter mooring lines that will stiffen the structure, bringing the natural frequency closer to the wave excitation range. This will happen

for all the DoFs, but it mostly concerns the compliant ones (see Section 2.3). This phenomenon can be mitigated by reducing the excess buoyancy. Reducing the tension in the mooring lines would steer the natural

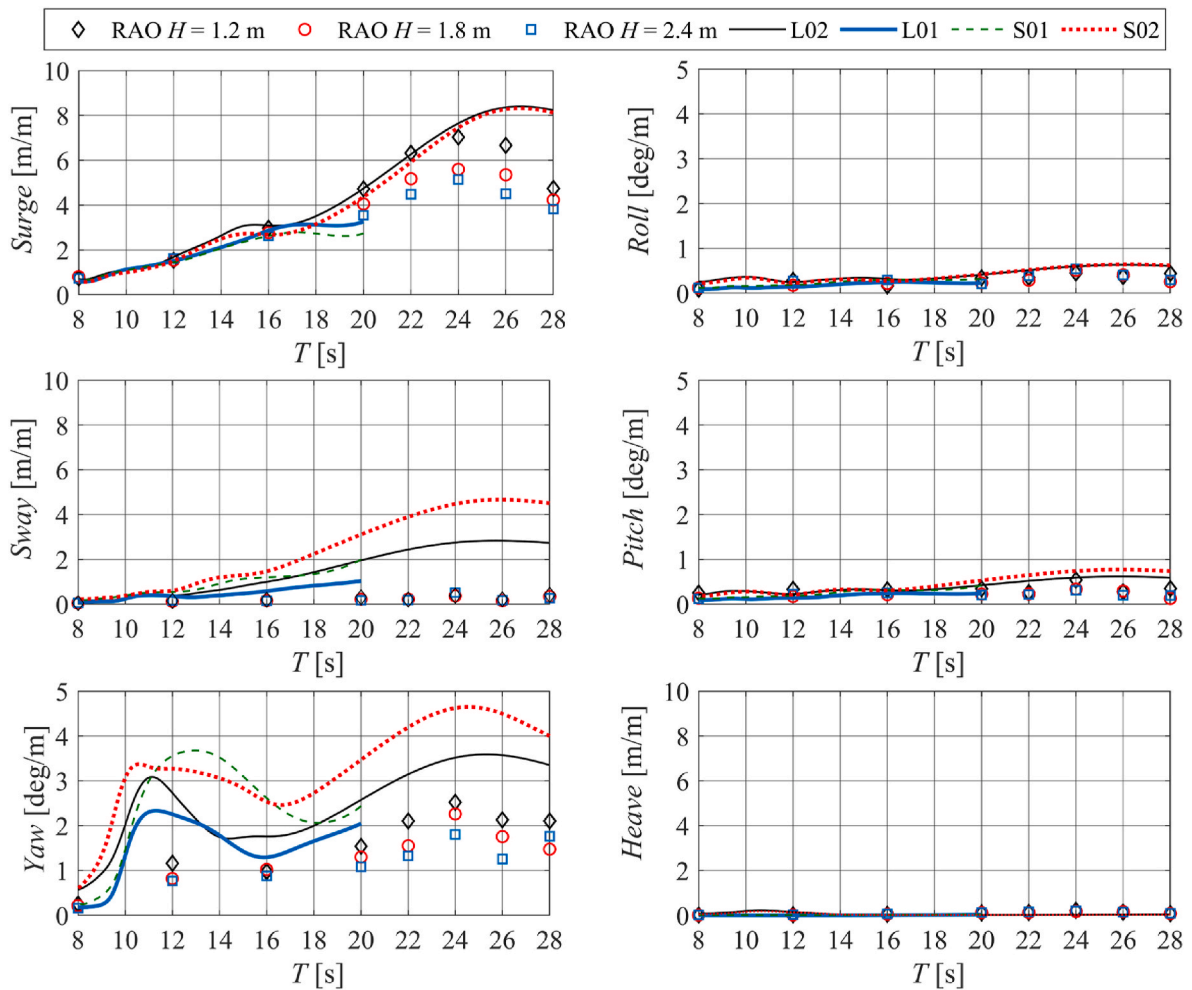


Fig. 15. RAOs and transfer functions of the device (prototype scale).

frequency back to safer values. While managing the excess of buoyancy could enhance the dynamic response of the structure, it is essential to strike a balance, as excessively reducing the buoyancy surplus will decrease the magnitude of the restoring forces against surge motions. An alternative, albeit more expensive, solution involves simultaneously ballasting the structure and increasing buoyancy, maintaining mooring line tension while shifting the natural frequency to safer values. Nevertheless, deploying this device in very shallow waters is not advisable, considering both response dynamics and the feasibility of seabed fixation.

The sway RAO, as expected for the analysed wave heading, presents very low values below 0.4 m/m in prototype scale. Given the symmetrical properties of this device, the sway response should closely resemble the surge counterpart for a perpendicular wave heading. The non-zero values of this RAO result from the slight deviations in the trajectories, which are more pronounced for the test cases with higher surge responses (see Fig. 14).

The heave RAO exhibits minimal values, all under 0.2 m/m, as expected from a TLP platform. The mooring lines of HelioSea impede upward motions from the equilibrium position, and the buoyancy excess greatly hinders downward motion. The stiffness of the device impedes resonance through ocean wave excitation (see Table 4). The subtle witnessed heave motions are not directly provoked by the fluctuation of wave-induced pressures on the structure but rather result from the surge motions, since the device must follow the arc of the mooring lines. Hence, the heave RAOs mirror the trend observed in the surge RAOs, albeit with markedly smaller responses. Note that shorter mooring lines

would suggest increased heave motions, but to a very limited extent. This restricted heave response, resulting from the inherent nature of the TLP design, could prove beneficial for easier maintenance of the device.

Both pitch and roll motions are heavily restricted by the mooring system. Again, the stiffness of the mooring lines against these motions impedes resonance (see Table 4), and so it is evidenced by the RAOs, with values lower than 0.5 deg/m. In these tests, pitch/roll motions arise from minor instabilities linked to the device's excursions and oscillate at low frequencies, distanced from resonance. The minimal pitch and roll responses are a distinguishing feature of the HelioSea design, in contrast to conventional multibody pontoon-type FPVs. The latter can present resonant, pitch amplitudes of up to 15 deg under wave heights lower than 1 m, and display panel misalignments of up to 10 deg for frequencies far from resonance (Delacroix et al., 2023). HelioSea succeeds in providing a stability that avoids resonance, mitigates misalignment losses, and allows the operation of a horizontal tracking system to promote efficiency even further.

The yaw RAOs were low, reaching up to 1 deg/m for test cases with $T < 20$ s, and a maximum of 3 deg/m for test cases with higher periods. Given the overall flatness of the results, no discernible resonance can be extracted from the RAOs. Substantial yawing moments require the asymmetrical application of forces within the structure and a sufficiently long lever arm, which the slender design of HelioSea prevents. A potential enhancement to limit yaw further in future developments of HelioSea could involve reconfiguring the pontoons' cross-section to a slender beam with increased height. This redesign aligns with structural considerations as the pontoon primarily experiences flexural stresses

but, more importantly, increases the added mass in this DoF, thereby shifting the natural frequency away from the common wave frequencies. This may also favour hydrodynamic damping, limiting resonance amplification. Tuning the excess buoyancy as well as the distance between the post and the fairleads can also result in a more flexible system, but at the cost of diminishing the restoring moments, which may be required to resist wind-induced yaw.

In general terms, the device exhibits restrained responses, especially in test cases with $T < 20$ s, affirming the stability of HelioSea under common ocean wave conditions. This is as crucial as encouraging, both from a structural and a productivity standpoint. With minimal misalignment of panels, potential losses are mitigated, and the operation of tracking systems, particularly the horizontally oriented one which is more efficient, appears secure.

3.3. Motion response analysis in irregular waves

Irregular wave tests were carried out on HelioSea to verify the stability of this structure under more realistic conditions. The time series for the free surface elevation, as well as the captured motions of the device, are shown as an example in Fig. 16. As expected, surge motions continue to be dominant, while sway motions play a secondary role and heave motions are barely discernible. Yaw motions continue to dominate in rotational motions, given the comparatively lower significance of pitch and roll motions. Note that some wave periods favoured a deviation of the trajectory of the device (see Fig. 14). This could not be removed from the irregular tests since a complete sea state was to be analysed. These deviations are mostly responsible for the more pronounced sway and yaw motions.

In all irregular wave tests, the generated waves followed the previously defined JONSWAP spectrum. A comparison between the model spectrum and a spectrum generated with the data registered by WP5 (at the location of the device) for both tests is presented in Fig. 17. In all cases, the maximum measured wave height was around 2 m, in prototype scale, which is congruent with the defined $H_s = 1.2$ m. Note that, while the peak periods are perfectly aligned, the peak spectral density is slightly lower in the short-crested tests.

Transfer functions were obtained, for each of the irregular wave tests, through the motion response spectra and their corresponding wave spectra. These transfer functions are shown and compared to the previously obtained RAOs in Fig. 15. Note that the functions corresponding with tests L01 and S01 are not represented beyond $T = 20$ s, as there is minimal wave energy in the spectrum for that frequency range (Fig. 17).

Again, the compliant DoFs (surge, sway, and yaw) result in the most noticeable responses. The surge transfer functions match the RAOs for $T < 20$ s while, for greater values of T , they reach slightly higher values. This deviation is probably explained by the partial linearity loss around resonance as well as the fact that wave reflection is more pronounced for the higher wave periods. Notwithstanding, the general tendency of the RAOs is followed by the transfer functions, peaking around the expected natural period.

The sway transfer functions are more pronounced than their corresponding RAOs. This phenomenon may be explained by the deviation of the trajectory of the device with time (see Fig. 14). This phenomenon is more pronounced for the tests with longer peak periods and short-crested waves, due to directional spreading. The heave transfer functions present very low values, with a slight mismatch in the highest frequencies, which is explained by the surge dependence of heave motions.

As for rotational motions, the roll and pitch irregular transfer functions match their corresponding RAOs for all the frequency domain. This result reaffirms the remarkable stability of HelioSea witnessed in the regular tests. As for the yaw transfer functions obtained with the results from the irregular wave tests, the response is greater than the response obtained through some of the regular tests. This may have the same explanation as the sway response, being influenced by trajectory deviations as well as the directional spreading of waves.

The maximum amplitudes of motion registered during the irregular wave tests are summarized in Table 9. The values are higher for test cases L02 and S02, in agreement with the obtained RAOs and transfer functions. Horizontal translational motions are the most prominent while heave, pitch, and roll motions are notably minimal, consistent with expectations. Yaw motions are greater in the presence of short-crested waves, and overall consistent with the transfer functions.

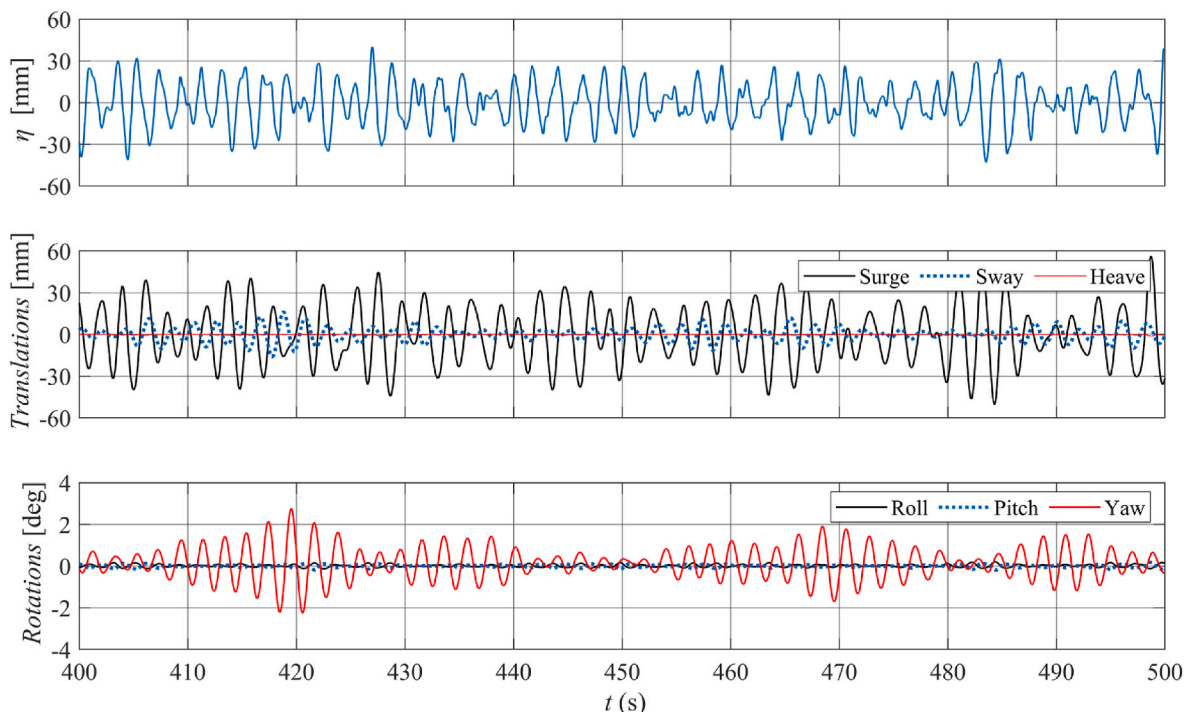


Fig. 16. Water surface elevation and motions of the device for L01 (model scale).

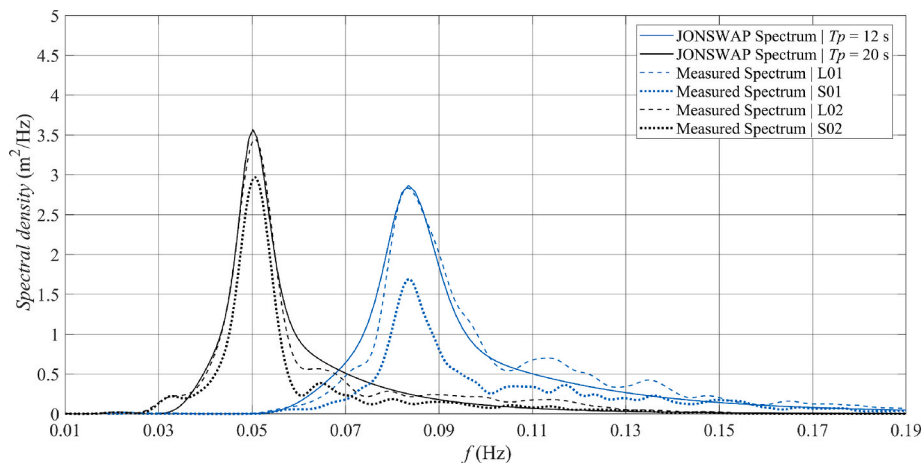


Fig. 17. Defined JONSWAP spectra and measured wave spectra for both irregular wave tests (prototype scale).

Table 9

Maximum amplitudes of motions registered in the irregular wave tests (prototype scale).

Test case	Surge [m]	Sway [m]	Heave [m]	Roll [deg]	Pitch [deg]	Yaw [deg]
L01	1.80	0.46	0.03	0.19	0.20	2.39
L02	3.84	1.97	0.08	0.48	0.46	3.03
S01	1.30	0.58	0.02	0.21	0.23	2.60
S02	3.69	2.60	0.10	0.53	0.50	3.20

In test cases L01 and S01, which are more representative of normal operating conditions, the device is very stable, and the production of solar panels should barely be affected by panel misalignment. Surge motions, reaching a maximum of 1.8 m on prototype scale, are notably low given the actual size of the structure. This excursion would imply a mooring line angle of 2.3 deg, well below the recommended limit of 10 deg. This low maximum surge implies a much smaller maximum heave of up to 0.03 m on prototype scale. Notably, both pitch and roll exhibit exceptionally low maximum motions, measuring at 0.21 and 0.23 deg, respectively. This would imply minimal panel misalignment losses, reinforcing further the claims already made in this regard. Yaw motions are also quite reduced, reaching a maximum value of 2.60 deg.

4. Conclusions

This paper presents the experimental evaluation of HelioSea, a novel FPV device tailored for marine environments. The technology features a pole-mounted solar platform with a double-axis tracker, supported by a tension leg platform (TLP) anchored to the seabed with cables. Extensive testing was conducted in the wave basin of the University of Porto with a 1:30 scale model. A piston-type wave maker was used to generate regular and irregular wave conditions, including long and short-crested spectra. The water surface elevation oscillations were measured with a layout of resistive-type wave probes, and the motions of the device were captured with an infrared motion capture system.

A total of 27 regular tests were carried out to determine the motion response of the structure to waves. As expected for a TLP, the motions in the horizontal plane (surge, sway, and yaw), were predominant over the motions in the vertical plane (roll, pitch, and heave), which were heavily restricted by the stiffness of the mooring system. Surge motions presented a subdued response below 4 m/m for typical wave conditions, with a natural frequency near $T = 24$ s on prototype scale. This value closely matches previous estimations and falls outside of the common ocean wave frequency range. The response exhibited a linear and consistent behaviour. Sway motions were minimal, due to the wave

heading. Heave motions, restricted by the mooring lines, mirror the trend observed in the surge RAOs, albeit with markedly smaller responses, all below 0.2 m/m. Pitch and roll motions were also heavily restricted by the stiffness of the system, exhibiting amplitudes lower than 0.5 deg/m under typical wave conditions. Yaw motions, although compliant with the structure, maintained a response amplitude below 1 deg/m under common wave conditions. The general response of the device for test cases with $T < 20$ s was quite limited, which proves the stability of the structure in typical operating conditions.

Tests with irregular sea-states were conducted to assess the device's performance under realistic wave conditions and calculate its motion transfer functions. Most of these functions closely align with the results obtained in the regular response analysis, further reinforcing the established claims. The sway and yaw transfer functions exhibited slightly higher values, influenced by the directional spread of waves and deviations in the device's trajectory. The maximum motion amplitudes recorded during the irregular wave tests underscore the device's exceptional stability under operational conditions. This remarkable aspect of HelioSea is as crucial as encouraging, both from a structural and a productivity standpoint. Rotational motions are very low, preventing panel misalignment losses and ensuring the efficient operation of the solar tracking system. The insights resulting from these tests will guide the future developments of HelioSea, including but not limited to design adaptations to shallower conditions and further controlling yaw rotations through adjustments in excess buoyancy, mooring line configuration, and redesigning of the pontoons' cross-section.

Future research will focus on calibrating a numerical model using the data gleaned from these experimental tests. Additionally, efforts will be made to estimate the impact of wind and current loads on the device, allowing for a comprehensive analysis of its response under operational and extreme marine environmental conditions.

CRediT authorship contribution statement

Rubén Claus: Data curation, Formal analysis, Investigation, Writing – original draft, Conceptualization, Methodology, Software. **Fernando Soto:** Data curation, Investigation, Writing – review & editing, Software. **Alejandro Cebada:** Data curation, Investigation, Writing – review & editing. **Mario López:** Conceptualization, Formal analysis, Funding acquisition, Investigation, Methodology, Supervision, Writing – review & editing. **Daniel Clemente:** Investigation, Methodology, Supervision, Writing – review & editing. **Gianmaria Giannini:** Methodology, Project administration, Supervision, Writing – review & editing. **Paulo Rosa-Santos:** Funding acquisition, Methodology, Project administration, Resources, Supervision, Writing – review & editing.

Declaration of competing interest

The authors declare that they have no known competing financial interests or personal relationships that could have appeared to influence the work reported in this paper.

Data availability

Data will be made available on request.

Acknowledgements

This work was supported by the PORTOS project co-financed by the Interreg Atlantic Area Programme through the European Regional Development Fund [grant number EAPA_784/2018]. During this work, R. Claus was supported by the “Programa Severo Ochoa de Ayudas para la investigación y docencia”, a research fellowship programme financed by the Government of the Principality of Asturias (Spain) [grant number AYUD0029T01]. A. Cebada was supported by the “Ayudas para realización de Tesis Doctorales. Modalidad A: Contratos de Investigación en régimen de concurrencia competitiva”, a research fellowship programme financed by the University of Oviedo (Spain) [grant number PAPI-21-PF-31]. G. Giannini gratefully acknowledges the financial support received through the Stimulus of Scientific Employment program of the Portuguese Foundation of Science and Technology (FCT), specifically via an individual grant referenced 2022.04954.CEECIND/CP1728/CT0007.

Furthermore, all authors would like to extend their sincere appreciation to Mr. Miguel Guerra for his assistance in conducting the experimental testing of HelioSea.

References

- Bachynski, E.E., Moan, T., 2012. Design considerations for tension leg platform wind turbines. *Mar. Struct.* 29, 89–114. <https://doi.org/10.1016/j.marstruc.2012.09.001>.
- Baquerizo, A., 1995. *Wave Reflection on Beaches: Methods of Assessment and Forecasting*. Ph. D. Thesis.
- Bugeja, R., Mule' Stagno, L., Branche, N., 2021. The effect of wave response motion on the insolation on offshore photovoltaic installations. *Sol. Energy Adv.* 1, 100008 <https://doi.org/10.1016/j.seja.2021.100008>.
- Cazzaniga, R., Rosa-Clot, M., 2021. The booming of floating PV. *Sol. Energy* 219, 3–10. <https://doi.org/10.1016/j.solener.2020.09.057>.
- Cazzaniga, R., Cicu, M., Rosa-Clot, M., Rosa-Clot, P., Tina, G.M., Ventura, C., 2018. Floating photovoltaic plants: performance analysis and design solutions. *Renew. Sustain. Energy Rev.* 81, 1730–1741. <https://doi.org/10.1016/j.rser.2017.05.269>.
- Chakrabarti, S.K., 1987. *Hydrodynamics of Offshore Structures*. WIT press.
- Chakrabarti, S., 2005. *Handbook of Offshore Engineering (2-volume Set)*. Elsevier.
- Claus, R., López, M., 2022. Key issues in the design of floating photovoltaic structures for the marine environment. *Renew. Sustain. Energy Rev.* 112502.
- Claus, R., López, M., 2023. A methodology to assess the dynamic response and the structural performance of floating photovoltaic systems. *Sol. Energy* 262, 111826. <https://doi.org/10.1016/j.solener.2023.111826>.
- Delacroix, S., Bourdier, S., Soulard, T., Elzaabalawy, H., Vasilenko, P., 2023. Experimental modelling of a floating solar power plant array under wave forcing. *Energies* 16. <https://doi.org/10.3390/en16135198>.
- Duck, Solar, 2021. *Unique Solution Solar Duck* [WWW Document]. URL <https://solarduck.tech/unique-solution/>, 9.1.23.
- Elminshawy, N.A.S., Osama, A., El-Damhogi, D.G., Oterkus, E., Mohamed, A.M.I., 2021. Simulation and experimental performance analysis of partially floating PV system in windy conditions. *Sol. Energy* 230, 1106–1121. <https://doi.org/10.1016/j.solener.2021.11.020>.
- Fernandez, H., Iglesias, G., Carballo, R., Castro, A., Fraguela, J.A., Taveira-Pinto, F., Sanchez, M., 2012. The new wave energy converter WaveCat: concept and laboratory tests. *Mar. Struct.* 29, 58–70. <https://doi.org/10.1016/j.marstruc.2012.10.002>.
- Friel, D., Karimirad, M., Whittaker, T., Doran, J., 2023. Experimental hydrodynamic assessment of a cylindrical-type floating solar system exposed to waves. *J. Ocean Eng. Sci.* <https://doi.org/10.1016/j.joes.2023.08.004>.
- Garanovic, A., 2021. *Equinor to Test Floating Solar Pilot in Rough Waters of Norway* [WWW Document]. Offshore Energy. URL <https://www.offshore-energy.biz/equinor-to-test-floating-solar-pilot-in-rough-waters-of-norway/>, 2.10.21.
- Hughes, S.A., 1993. *Physical Models and Laboratory Techniques in Coastal Engineering*. World Scientific.
- Ikhennicheu, M., Blanc, A., Danglade, B., Gilloteaux, J.-C., 2022. OrcaFlex modelling of a multi-body floating solar island subjected to waves. *Energies* 15, 9260.
- Jiang, Z., Dai, J., Saetone, S., Tørå, G., He, Z., Bashir, M., Souto-Iglesias, A., 2023. Design and model test of a soft-connected lattice-structured floating solar photovoltaic concept for harsh offshore conditions. *Mar. Struct.* 90 <https://doi.org/10.1016/j.marstruc.2023.103426>.
- Kazem, H.A., Chaichan, M.T., Alwaeli, A.H., Mani, K., 2017. Effect of shadows on the performance of solar photovoltaic. In: *Mediterranean Green Buildings & Renewable Energy: Selected Papers from the World Renewable Energy Network's Med Green Forum*, pp. 379–385.
- Kurniawan, A., Grassow, M., Ferri, F., 2019. Numerical modelling and wave tank testing of a self-reacting two-body wave energy device. *Ships Offshore Struct.* 14, 344–356.
- Lavelle, J., Kofoed, J.P., 2011. Experimental testing of the Langlee wave energy converter. In: *Proceedings of the 9th European Wave and Tidal Energy Conference*, pp. 5–9. Southampton, UK.
- López, M., Rodríguez, N., Iglesias, G., 2020. Combined floating offshore wind and solar PV. *J. Mar. Sci. Eng.* 8 <https://doi.org/10.3390/JMSE8080576>.
- López, M., Soto, F., Hernández, Z.A., 2022. Assessment of the potential of floating solar photovoltaic panels in bodies of water in mainland Spain. *J. Clean. Prod.* 340, 130752 <https://doi.org/10.1016/j.jclepro.2022.130752>.
- Mani, M., Pillai, R., 2010. Impact of dust on solar photovoltaic (PV) performance: research status, challenges and recommendations. *Renew. Sustain. Energy Rev.* 14, 3124–3131.
- Mansard, E.P.D., Funke, E.R., 1980. The measurement of incident and reflected spectra using a least squares method. *Coast Eng.* 1980, 154–172.
- Nsengiyumva, W., Chen, S.G., Hu, L., Chen, X., 2018. Recent advancements and challenges in solar tracking systems (STS): a review. *Renew. Sustain. Energy Rev.* 81, 250–279. <https://doi.org/10.1016/j.rser.2017.06.085>.
- DEMETractable, Nul, J. De, 2023. *SeaVolt* [WWW Document]. URL <https://www.seavolt.be/>, 9.1.23.
- Oceans of Energy, 2020. *Offshore Floating Solar Farm Installed and Operational at the Dutch North Sea System Survived Several Storms, Including the “Ciara” Storm*. February 2020 [WWW Document]. Ocean Energy. URL <https://oceansofenergy.blue/north-sea-1-offshore-solar-project/>, 5.7.20.
- Oguz, E., Clelland, D., Day, A.H., Incecik, A., López, J.A., Sánchez, G., Almeria, G.G., 2018. Experimental and numerical analysis of a TLP floating offshore wind turbine. *Ocean Eng.* 147, 591–605. <https://doi.org/10.1016/j.oceaneng.2017.10.052>.
- Oliveira-Pinto, S., Stokkermans, J., 2020. Marine floating solar plants: an overview of potential, challenges and feasibility. *Proc. Inst. Civ. Eng. Marit. Eng.* 173, 120–135. <https://doi.org/10.1680/jmaen.2020.10>.
- Qualisys, 2017. *Qualisys Track Manual: User Manual*.
- Rosa-Santos, P., Taveira-Pinto, F., López, M., Rodríguez, C.A., 2022. Hybrid systems for marine energy harvesting. *J. Mar. Sci. Eng.* 10 <https://doi.org/10.3390/jmse10050633>.
- Sheng, W., 2019. Wave energy conversion and hydrodynamics modelling technologies: a review. *Renew. Sustain. Energy Rev.* 109, 482–498. <https://doi.org/10.1016/j.rser.2019.04.030>.
- Siddiqui, N.A., Ahmad, S., 2001. Fatigue and fracture reliability of TLP tethers under random loading. *Mar. Struct.* 14, 331–352. [https://doi.org/10.1016/S0951-8339\(01\)00005-3](https://doi.org/10.1016/S0951-8339(01)00005-3).
- Sun, Ocean, 2017. *A unique solution to floating solar* [WWW Document]. URL <https://oceansun.no/>, 2.22.21.
- Sun, X., Silverman, T.J., Zhou, Z., Khan, M.R., Bermel, P., Alam, M.A., 2017. Optics-based approach to thermal management of photovoltaics: selective-spectral and radiative cooling. *IEEE J. Photovoltaics* 7, 566–574. <https://doi.org/10.1109/JPHOTOV.2016.2646062>.
- Sun, X., Khan, M.R., Deline, C., Alam, M.A., 2018. Optimization and performance of bifacial solar modules: a global perspective. *Appl. Energy* 212, 1601–1610. <https://doi.org/10.1016/j.apenergy.2017.12.041>.
- Tina, G.M., Bontempo Scavo, F., Merlo, L., Bizzarri, F., 2021. Comparative analysis of monofacial and bifacial photovoltaic modules for floating power plants. *Appl. Energy* 281, 116084. <https://doi.org/10.1016/j.apenergy.2020.116084>.
- Ueda, Y., 2008. Performance analysis of pv systems on the water. In: *23rd European Photovoltaic Solar Energy Conference*, pp. 1–5. Valencia, Spain.
- Yang, R.-Y., Yu, S.-H., 2021. A study on a floating solar energy system applied in an intertidal zone. *Energies* 14, 7789.
- Yihe, X., 2023. *CIMC Raffles Delivers China's First Floating Solar Power Platform* [WWW Document]. Upstream. URL <https://www.upstreamonline.com/energy-transition/cimc-raffles-delivers-china-s-first-floating-solar-power-platform/2-1-1431673,9.1.23>.